whichever is shorter. Since the reflection strength for all N beams is very low, the self-extinction depth is quite large.

We calculated the $I(\theta)$ curve as F_{622} approached zero. As F_{622} becomes smaller, $E_{\rm mult}$ is virtually unchanged and there remains a narrow rocking curve at the 622 position whose strength is determined by the excitation of the N beams. There is no general background scattering in reciprocal space because of n-beam effects. What appears is a node of reflectivity at the reciprocal-lattice point even as the structure factor F_{622} goes to zero.

These results indicate that even extremely weak multiple-beam effects cannot be treated kinematically. There is a dynamical interaction of beams whenever a Bragg condition is satisfied, *i.e.* wherever $\mathbf{k}_f$ in Fig. 1 is at a node of the reciprocal lattice.

When a dynamical reflection is extremely weak, the integrated intensity for a given F is the same as that calculated from the kinematic expression, which is proportional to F^2. However, the interaction of the beams is clearly dynamic in origin. For any region of k space near a reciprocal-lattice point, the scattered intensity contributed by each of the N beams is essentially zero because we are so far removed from satisfying the Bragg condition for those reflections. However, if the $\mathbf{k}_f$ vector approaches a node of the reciprocal lattice, even if the node has a zero structure factor, a sharp, albeit weak, reflection will appear.

We investigated the general strength of the n-beam effect as a function of the atomic number Z. We calculated n-beam integrated intensities for the 622 reflection, at identical φ and λ/a_0. In the I region of Ge, $E^{\rm Ge}_{\rm mult}=0{\cdot}038$, and in the corresponding region of Si, $E^{\rm Si}_{\rm mult}=0{\cdot}0075$. The ratio of $E^{\rm Ge}_{\rm mult}/E^{\rm Si}_{\rm mult}=5{\cdot}07$, which is very close to the ratio $(Z_{\rm Ge}/Z_{\rm Si})^2$. Thus, the intensity of multiple-beam contributions for the two materials scales as Z^4. This explains why multiple-beam effects are much more important in Ge than Si and is consistent with our experimental results reported in Tischler & Batterman (1984). It appears that a simple condition governs the weak multiple-beam contributions; each pair of reflections satisfying $\mathbf{H}'+\mathbf{H}''=\mathbf{H}$ contributes as the product of the two intensities as if they were sequential reflections.

References

COLELLA, R. (1974). *Acta Cryst.* A**30**, 413-423.
RENNINGER, M. Z. (1937). *Z. Phys.* **106**, 141-176.
RENNINGER, M. Z. (1960) *Z. Kristallogr.* **113**, 99-103.
TISCHLER, J. Z. & BATTERMAN, B. W. (1984). *Phys. Rev. B*, **30**, 7060-7066.
WARREN, B. E. (1969). *X-ray Diffraction*, p. 46. Reading, MA: Addison-Wesley.

Acta Cryst. (1986). A**42**, 514-525

Determination of the Velocity of Sound in Crystals by Time-of-Flight Neutron Diffraction

BY B. T. M. WILLIS

Chemical Crystallography Laboratory, University of Oxford, 9 Parks Road, Oxford OX1 3PD, England; and Atomic Energy Research Establishment, Harwell, Oxon OX11 0RA, England

(*Received* 26 *February* 1986; *accepted* 8 *May* 1986)

Abstract

In a neutron Laue (time-of-flight) experiment, the nature of the thermal diffuse scattering by elastic waves depends on the ratio, β, of the sound velocity in the crystal to the neutron velocity. For slower-than-sound neutrons, there is a certain range of β for which a 'wavelength window' appears in the incident beam; TDS is forbidden for all wavelengths lying within this window. The window is best observed in back scattering, and for a scattering angle close to 180° the centre of the window coincides with the Bragg wavelength. At the edges of the window, the TDS intensity rises abruptly to two sharp peaks, one due to phonon emission and the other to phonon absorption. The sound velocity is derived by measuring the time of flight of either peak. The method is illustrated by applying it to pyrolytic graphite, which was examined using the neutron spallation source ISIS.

Glossary of symbols

$b_\kappa^{\rm coh}$	coherent scattering length of atom κ
$\mathbf{B}$	reciprocal-lattice vector
c_g	group velocity of sound
c_s	phase velocity of sound
$\mathbf{e}(\kappa \mid j\mathbf{q})$	polarization vector of atom κ excited by mode of vibration $(j\mathbf{q})$
E_0, E	initial and final energies of neutron
$G_j(\mathbf{Q})$	structure factor for one-phonon scattering
$\hbar$	Planck's constant/2π

0108-7673/86/060514-12$01.50

j	polarization index of normal mode
$\mathbf{k}_0, \mathbf{k}$	initial and final wave vectors of neutron
$\mathbf{k}_e$	vector along scattering direction of magnitude $\|\mathbf{k}_0\|$
k_B	$2\pi/\lambda_B$
Δk_0	$k_0 - k_B$
Δk	$k - k_B$
k'_B	Boltzmann's constant
L_0	distance from source to sample
L	distance from sample to detector
m_n	neutron mass
N	number of unit cells in crystal
$n_j(\mathbf{q})$	quantum number of normal mode $(j\mathbf{q})$
$\mathbf{q}$	wave vector of normal mode
$\mathbf{Q}$	scattering vector $(=\mathbf{k}-\mathbf{k}_0)$
$\mathbf{Q}_\theta^{el}$	vector defining locus of elastic scattering through angle 2θ
$\mathbf{r}_\kappa$	position of κth atom in unit cell
t	time of flight
t_B	time of flight for Bragg scattering
Δt	$t - t_B$
v_n	neutron velocity
v_0	volume of unit cell
W_κ	exponent of temperature factor of atom κ
β	c_s/v_n
β_g	c_g/v_n
ε	index for phonon absorption (-1) or phonon emission $(+1)$
ε'	$\varepsilon\Delta\theta/\|\Delta\theta\|$
$\boldsymbol{\eta}$	vector joining end points of $\mathbf{B}$ and $\mathbf{k}_e$
θ	half the scattering angle
θ_B	Bragg angle
$\Delta\theta$	$\theta - \theta_B$
κ	label for atom in unit cell
λ_B	Bragg wavelength
ξ	angle between $\mathbf{k}$ and $\boldsymbol{\eta}$
$\frac{d^2\sigma}{d\Omega\, dE}$	differential scattering cross section for solid angle $d\Omega$ and energy dE
ζ	angle between $\mathbf{B}$ and $\mathbf{q}$
χ	angle between $\mathbf{k}$ and $\text{grad}_\mathbf{q}\,\omega(\mathbf{q})$
$\omega_j(\mathbf{q})$	frequency of normal mode $(j\mathbf{q})$

1. Introduction

The purpose of this paper is to present the theory underlying a new method, which employs pulsed neutrons and time-of-flight diffraction, of measuring the velocity of sound in crystals. It promises to be of general application to crystals of any symmetry, even when examined under extreme conditions of pressure and temperature.

The theory hinges on the properties of the 'scattering surfaces' for the elastic and inelastic scattering of thermal neutrons. These surfaces are defined in § 2, where we show that the surfaces are fundamentally different for fixed-wavelength and for time-of-flight diffraction. These differences can be exploited in the time-of-flight case to derive sound velocities.

The diffraction method of studying excitations in crystals, employing neutron inelastic scattering without energy analysis, is not new. It was suggested originally by Elliott & Lowde (1955) for measuring spin-wave dispersion relations in magnetic materials with a neutron source of fixed wavelength. We shall describe the extension of the diffraction method to the determination of sound velocities with a 'white' source of pulsed neutrons.

2. One-phonon scattering surface in time-of-flight diffraction

The scattering surface is the locus in reciprocal space of the end points of the wave vectors $\mathbf{k}$ of neutrons which are scattered inelastically in a one-phonon process. To understand its properties, it is helpful to consider first the simpler case of the elastic scattering surface.

For elastic scattering - which includes Bragg scattering - there is no change of energy or wavelength on scattering, *i.e.*

$$k = k_0 \tag{1}$$

where k_0 and k are the magnitudes of the wave vectors of the incident and scattered beams respectively. In a fixed-wavelength experiment, the scattering angle 2θ is a continuous variable, and the scattering surface defined by (1) is the *Ewald sphere* (Fig. 1*a*). On the other hand, in time-of-flight diffraction, 2θ is kept fixed and the incident wavelength varies; the scattering surface is then a *right-circular cone* with its axis along the incident beam and with semi-angle $(\pi/2)-\theta$ (Fig. 1*b*).

The geometry of the one-phonon scattering surface is determined by the conservation relations for energy and momentum, when the neutron exchanges one quantum (phonon) of energy with the crystal. Let $\hbar\omega_j(\mathbf{q})$ be the phonon energy, where ω is the frequency and j labels the branch of the dispersion curves. ($\hbar = h/2\pi$.) $\mathbf{q}$ is the wave vector of the normal mode of vibration; as $q \to 0$, the three acoustic modes $(j = 1, 2, 3)$ are identified as the three sound waves with the same propagation vector $\mathbf{q}$.

The conservation of momentum for a one-phonon process with neutron-energy gain (phonon absorption) is expressed by

$$\mathbf{k} - \mathbf{k}_0 = \mathbf{B} + \mathbf{q} \tag{2}$$

where $\mathbf{B}$ is the reciprocal-lattice vector (*i.e.* $\hbar\mathbf{B}$ is the momentum taken up by the crystal). The magnitude of $\mathbf{k}_0$ is related to the wavelength λ in the incident white beam by

$$k_0 = 2\pi/\lambda,$$

and if λ_B is the wavelength giving rise to Bragg

scattering at $\theta = \theta_B$, then

$$\lambda_B = 4\pi \sin\theta_B / |\mathbf{B}|.$$

Equation (2) is illustrated by the vector diagram, Fig. 2, in which $\overrightarrow{AQ}$ is $\mathbf{k}$, $\overrightarrow{AO}$ is $\mathbf{k}_0$, $\overrightarrow{OP}$ is $\mathbf{B}$ and $\overrightarrow{PQ}$ is $\mathbf{q}$. Extending the equation to include the energy-loss process:

$$\mathbf{k} - \mathbf{k}_0 = \mathbf{B} - \varepsilon\mathbf{q} \qquad (3)$$

where ε is either $+1$ or -1. $\varepsilon = +1$ refers to phonon emission and $\varepsilon = -1$ to phonon absorption.

The conservation of energy on scattering is expressed as

$$(\hbar^2/2m_n)(k^2 - k_0^2) = -\varepsilon\hbar\omega(\mathbf{q})$$

with m_n the neutron mass. This can be rewritten in the form

$$(\hbar/2m_n)(k - k_0)[(\Delta k + \Delta k_0) + 2k_B] = -\varepsilon\omega(\mathbf{q}) \qquad (4)$$

where

$$\Delta k = k - k_B, \qquad \Delta k_0 = k_0 - k_B, \qquad k_B = 2\pi/\lambda_B.$$

For scattering with small energy transfer ($q \to 0$), we can neglect the term $(\Delta k + \Delta k_0)$ in (4). This is the same approximation as that adopted by Seeger & Teller (1942) and later workers in discussing the fixed-wavelength case; the effect of this approximation is assessed later in § 6. In a diffraction experiment the neutron velocity, v_n, for Bragg scattering is $\hbar k_B/m_n$; and if the acoustic modes propagate at the phase velocity c_s without dispersion, then

$$\omega = c_s q. \qquad (5)$$

Hence (4) reduces to

$$k - k_0 = -\varepsilon\beta(\zeta)q \qquad (6)$$

where $\beta(\zeta) = c_s(\zeta)/v_n$. ζ is the angle between the

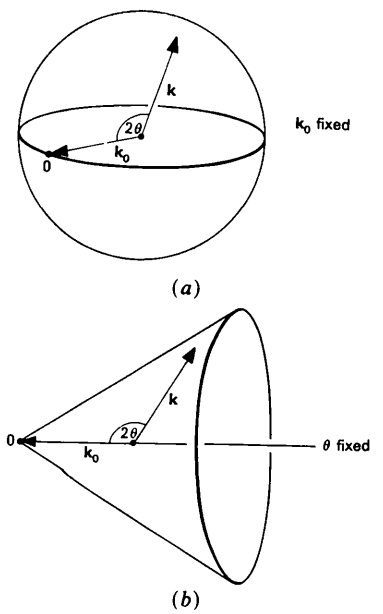

Fig. 1. Scattering surfaces for the elastic scattering of neutrons, X-rays *etc.* (*a*) Fixed wavelength and variable scattering angle, 2θ: *Ewald sphere.* (*b*) Fixed angle and variable wavelength: *right-circular cone.* (*a*) corresponds to conventional neutron or X-ray diffraction, whereas (*b*) refers to Laue or time-of-flight diffraction. *O* is the origin of reciprocal space. Bragg scattering occurs when the vector $\mathbf{k} - \mathbf{k}_0$ coincides with a reciprocal-lattice vector.

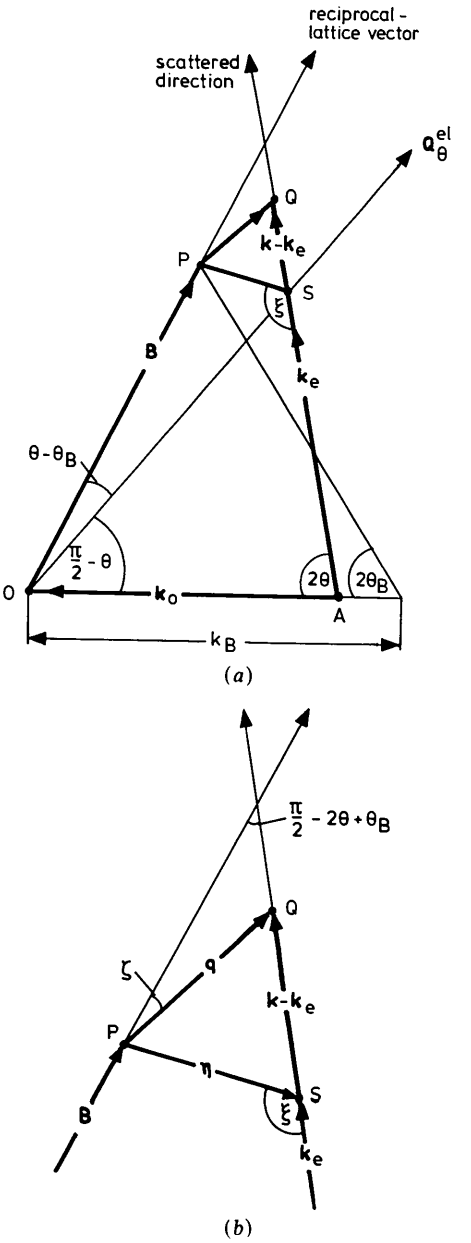

Fig. 2. (*a*) Vector diagram for scattering process involving the absorption of a phonon of energy $\hbar\omega(\mathbf{q})$ by the scattered neutron. $\mathbf{k}_e$ ($= \overrightarrow{AS}$) is a vector in the scattering direction having the same length as the incident wave vector $\mathbf{k}_0$ ($= \overrightarrow{AO}$). $\overrightarrow{AQ}$ is the scattered wave vector $\mathbf{k}$, and $\boldsymbol{\eta}$ is the vector joining the end points of $\mathbf{k}_e$ and the reciprocal-lattice vector $\mathbf{B}$. The length of $\overrightarrow{PQ}$ is q and of $\overrightarrow{SQ}$ is βq. (In this and later diagrams *O* is the origin of reciprocal space.) (*b*) shows triangle *PQS* enlarged.

phonon wave vector $\mathbf{q}$ and the reciprocal-lattice vector $\mathbf{B}$ (see Fig. 2). Nearly all crystals are elastically anisotropic, and so the phase velocity and the velocity ratio β are functions of the angle ζ. Our treatment applies to anisotropic crystals, but we shall assume isotropic behaviour (for example, in Figs. 4, 5 and 8) where this assumption does not invalidate the main argument. In the final section the velocity of sound is derived for pyrolytic graphite, which is highly anisotropic.

Equation (6) determines the topology of the one-phonon scattering surfaces. This topology is quite different according to whether or not the condition for Bragg scattering, $2\theta = 2\theta_B$, is satisfied.

(i) $\theta = \theta_B$

Let us consider first the geometry in reciprocal space (Fig. 3) for the measurement of Bragg intensities by neutron Laue diffraction. The incident beam possesses a band of wave vectors $\mathbf{k}_0$, represented by the vectors lying between $\overrightarrow{A_1O}$ and $\overrightarrow{A_2O}$. The angle of scattering is $2\theta_B$, where $(\pi/2)-\theta_B$ is the angle between $\mathbf{k}_0$ and the reciprocal-lattice vector $\overrightarrow{OP}$. If the length of $\overrightarrow{OP}$ is $|\mathbf{B}|$, the particular value of k_0 given by

$$k_0 = |\mathbf{B}|/(2\sin\theta_B)$$

(AO in Fig. 3) is Bragg reflected, but there is no reflection of the remaining wavelengths. The vector $\mathbf{Q}^{el}_{\theta_B}$ in Fig. 3 is the locus of *all* elastic scattering events and is the intersection in the scattering plane of the cone shown in Fig. 1(*b*).

Fig. 4 shows the one-phonon scattering surfaces in reciprocal space when $\theta = \theta_B$ and $\beta < 1$. Consider the region of the diagram with $\varepsilon = -1$ and $\Delta k_0 > 0$, *i.e.* where $k > k_0 > k_B$. $\overrightarrow{A_2O}$ is the vector $\mathbf{k}_0$ and $\overrightarrow{A_2Q}$ is the vector $\mathbf{k}$. Thus the length of $\overrightarrow{A_2Q}$ is

$$k_0 + \beta q,$$

from (6).

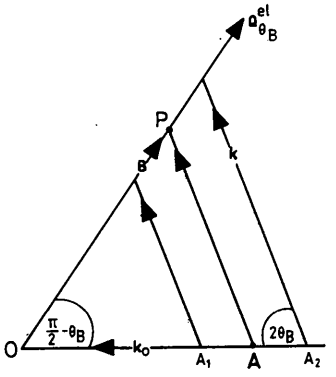

Fig. 3. Measurement of integrated intensity of Bragg reflection at P by neutron Laue diffraction. P is scanned, at a fixed scattering angle $2\theta_B$, by a variable wavelength $2\pi/k_0$. Bragg scattering occurs when $\mathbf{k}_0$ ($=\overrightarrow{AO}$) and $\mathbf{k}$ ($=\overrightarrow{AP}$) are equal to k_B where $k_B = \frac{1}{2}|\mathbf{B}|$ cosec θ_B.

Referring to the triangle PQS in Fig. 4, where S is the point of intersection of $\mathbf{Q}^{el}_{\theta_B}$ and $\mathbf{k}$, we have

$$q^2 = \eta^2 + \beta^2 q^2 - 2\varepsilon\beta q\eta \sin\theta_B \qquad (7)$$

in which η is the length of the vector $\overrightarrow{PS}$ ($=\boldsymbol{\eta}$). Equation (7) also applies to phonon emission, with $\varepsilon = +1$ and $\Delta k_0 > 0$, and its solution is

$$\eta/q = (\varepsilon\Delta k_0/|\Delta k_0|)\,\beta\sin\theta_B \pm (1-\beta^2\cos^2\theta_B)^{1/2}. \qquad (8)$$

Equation (8) has been generalized to include all four regions in Fig. 4 with $\varepsilon = \pm 1$ and $\Delta k_0 \lessgtr 0$.

The phonon wave number q in (8) must be both real and positive. The first condition requires that $\beta < \sec\theta_B$, and so if β exceeds $\sec\theta_B$ (*i.e.* if the neutron velocity is less than $\cos\theta_B$ times the sound velocity) there is no one-phonon scattering. The absence of TDS from crystals examined with very slow neutrons provides a method of measuring Bragg intensities, *which are free from contamination by thermal scattering.*

The second condition is that q must be positive. Consider the following possible values of η/q:

$$\left.\begin{aligned}(a)\quad \eta/q &= \beta\sin\theta_B + (1-\beta^2\cos^2\theta_B)^{1/2}\\ (b)\quad \eta/q &= \beta\sin\theta_B - (1-\beta^2\cos^2\theta_B)^{1/2}\end{aligned}\right\}\frac{\varepsilon\Delta k_0}{|\Delta k_0|} = +1$$

$$\left.\begin{aligned}(c)\quad \eta/q &= -\beta\sin\theta_B + (1-\beta^2\cos^2\theta_B)^{1/2}\\ (d)\quad \eta/q &= -\beta\sin\theta_B - (1-\beta^2\cos^2\theta_B)^{1/2}\end{aligned}\right\}\frac{\varepsilon\Delta k_0}{|\Delta k_0|} = -1.$$

(a) is always positive, (b) is positive for $\beta > 1$, (c) is positive for $\beta < 1$, and (d) is always negative. Hence,

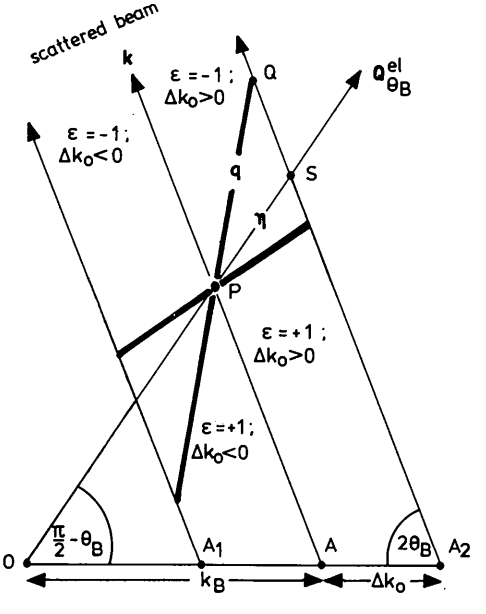

Fig. 4. One-phonon scattering surfaces (heavy lines) for $\theta = \theta_B$. P is the reciprocal-lattice point and the area in reciprocal space around P is divided into four regions by the crossed lines, representing the four combinations $\varepsilon = \pm 1$ and $k_0 - k_B \lessgtr 0$. The locus for elastic scattering, $k = k_0$, is the line along $\mathbf{Q}^{el}_{\theta_B}$.

if $\varepsilon\Delta k_0/|\Delta k_0| = +1$, there is one solution of q for $\beta < 1$, two solutions for $1 < \beta < \sec\theta_B$, and none for $\beta > \sec\theta_B$. If $\varepsilon\Delta k_0/|\Delta k_0| = -1$, there is one solution for $\beta < 1$ and none for $\beta > 1$.

Thus there are three distinct ranges of β to consider in a scattering experiment; $\beta < 1$, $1 < \beta < \sec\theta_B$, and $\beta > \sec\theta_B$. Fig. 5 illustrates the one-phonon scattering surfaces for these three ranges. For $\beta < 1$, Fig. 5(a), the surfaces form two arms of a cross, and the scattered wave vector $\mathbf{k}$ intersects the cross at both $\varepsilon = +1$ and $\varepsilon = -1$. For the range $1 < \beta < \sec\theta_B$, Fig. 5(b), the cross has moved to a different position in reciprocal space, so that the two scattering events associated with a given $\mathbf{k}_0$ are now either phonon absorption ($\Delta k_0 < 0$) or phonon emission ($\Delta k_0 > 0$) but not both. Finally, for $\beta > \sec\theta_B$, Fig. 5(c), the one-phonon scattering surface collapses to a single point at the lattice point P.

Fig. 6 shows schematically the TDS which is recorded near the Bragg peak in a time-of-flight experiment. The abscissa axis is labelled time of flight, t, which is related to Δk_0 by

$$\Delta k_0/k_0 = -(t - t_B)/t_B = -\Delta t/t_B$$

where t_B is the time of flight for Bragg scattering: see § 4. The TDS rises to a peak at $t = t_B$ for the two ranges $\beta < 1$ and $1 < \beta < \sec\theta_B$, and then suddenly vanishes for $\beta > \sec\theta_B$.

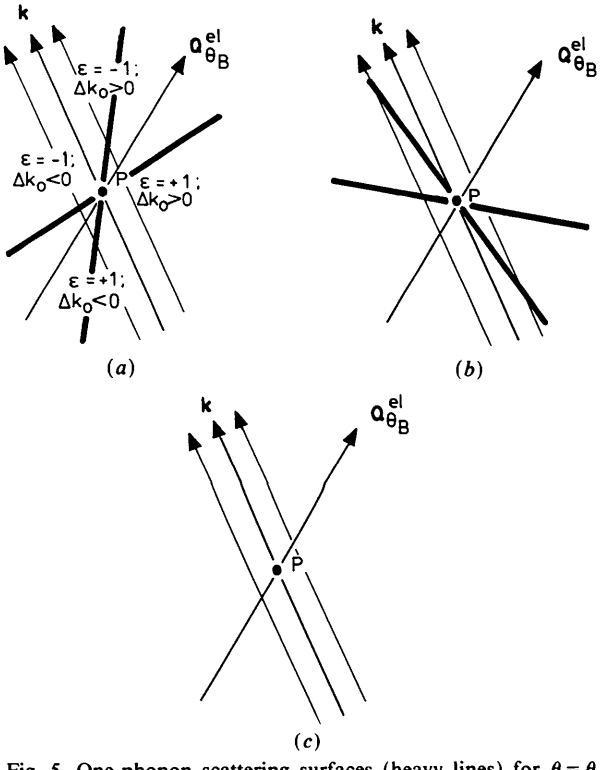

Fig. 5. One-phonon scattering surfaces (heavy lines) for $\theta = \theta_B$ and for the three ranges of the velocity ratio; (a) $\beta < 1$, (b) $1 < \beta < \sec\theta_B$, (c) $\beta > \sec\theta_B$.

(ii) $\theta = \theta_B + \Delta\theta$

The nature of the TDS in the three ranges of β is quite different when the detector is offset from the Bragg setting. The orientation of the crystal and the direction of the incident beam remain the same as in Fig. 3, but the detector is repositioned to receive radiation scattered at an angle 2θ where

$$\theta = \theta_B + \Delta\theta$$

and $\Delta\theta \ll \theta_B$ (see Fig. 7). The vector $\mathbf{Q}^{el}_{\theta}$, which is inclined at an angle $(\pi/2) - \theta$ to the incident radiation, represents the locus of elastically scattered events received by the detector. The lattice point P does not lie on this vector and so Bragg scattering is not observed.

If Q in Fig. 7 is the end-point of the scattered vector $\mathbf{k}$ for neutron energy gain ($\varepsilon = -1$), then $QS = \beta q$ and QN is $\beta q \cos\theta$, where N is the foot of the perpendicular from Q to the elastic scattering vector. Thus

$$QN/QP = \beta\cos\theta$$

and Q is constrained by the condition that the ratio of its distance from the fixed point P to its distance from the fixed line $\mathbf{Q}^{el}_{\theta}$ is equal to $(\beta\cos\theta)^{-1}$. If β is constant, *i.e.* the elastic waves propagate isotropically, the one-phonon scattering surface is a conic section whose eccentricity e is

$$e = (\beta\cos\theta)^{-1}. \qquad (9)$$

(In three dimensions, when the reciprocal-lattice point lies outside the scattering plane containing $\mathbf{k}_0$ and $\mathbf{k}$, the scattering surface is a conicoid. The eccentricity e is then defined as the ratio of the distance of Q from the point P to its distance from a plane which is normal to the scattering plane and contains $\mathbf{Q}^{el}_{\theta}$.)

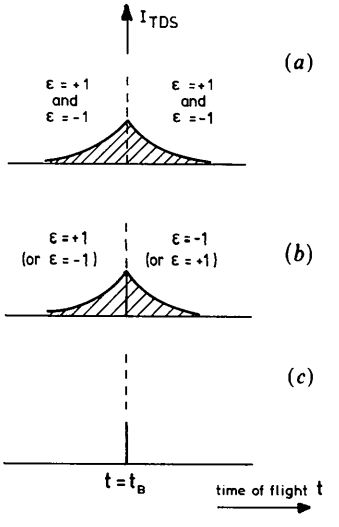

Fig. 6. Time dependence of the TDS intensity when $\theta = \theta_B$; (a) $\beta < 1$, (b) $1 < \beta < \sec\theta_B$, (c) $\beta > \sec\theta_B$.

For $e>1$ the scattering surface for isotropic crystals is a hyperboloid of two sheets with the reciprocal-lattice point at one focus; one sheet corresponds to $\varepsilon=-1$ and the other to $\varepsilon=+1$ (Figs. 8*a*,*b*,*c*). For $e<1$ the surface is an ellipsoid of revolution: only one scattering process is then possible, either phonon absorption if $\Delta\theta>0$ (Fig. 8*e*), or phonon emission if $\Delta\theta<0$.

3. The wavelength window

We shall show next that there is a range of incident wave numbers k_0 in the vicinity of k_B $(=2\pi/\lambda_B)$, which - under certain conditions - cannot satisfy the one-phonon conservation laws for energy and momentum. This 'wavelength window' in the incident white beam only occurs when the detector is offset from the Bragg setting at $\theta=\theta_B$.

From the triangle PQS in Fig. 2(*b*), we have

$$q^2=\eta^2+\beta^2q^2-2\varepsilon\beta q\eta\cos\xi \qquad (10)$$

where ξ is the angle between the vector $\overrightarrow{PS}$ $(=\boldsymbol{\eta})$ and the scattered direction. Equation (10) is identical with (7) for $\Delta\theta=0$, but with ξ replacing $(\pi/2)-\theta_B$.

The general solution of (10) is

$$q=\eta[\varepsilon'\beta\cos\xi\pm(1-\beta^2\sin^2\xi)^{1/2}]^{-1} \qquad (11)$$

where $\varepsilon'=\varepsilon\Delta\theta/|\Delta\theta|$. Both η and ξ in (11) are determined by the scattering angle and by the wavelength of the incident radiation.

Once again we will examine the implications of q being both real and positive, considering in turn the three ranges $\beta<1$, $1<\beta<\sec\theta$ and $\beta>\sec\theta$.

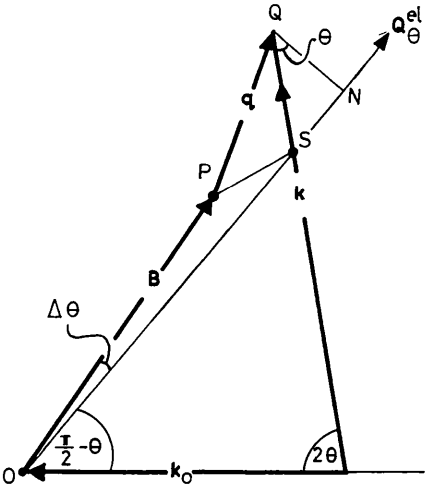

Fig. 7. The scattering angle has been increased by $2\Delta\theta$ compared with Fig. 3 for Bragg scattering. $\mathbf{Q}^{el}_{\theta}$ is the vector defining the locus of all elastic scattering events at the new scattering angle, and Q is the end point of the phonon wave vector $\mathbf{q}$. N is the foot of the perpendicular from Q to the elastic scattering line.

(i) $\beta<1$ [*see Fig.* 8(*a*)]

q in (11) is always real, but the positive root only is allowed for q to be positive. Thus there is just one solution for energy gain ($\varepsilon=-1$) and one for energy loss ($\varepsilon=+1$). There is no restriction on the angle ξ, which can lie anywhere in the range

$$(\pi/2)-\theta<\xi<(3\pi/2)-\theta,$$

and one-phonon scattering takes place, for absorption and emission, at any value of ξ within this range.

(ii) $1<\beta<\sec\theta$ [*see Fig.* 8(*c*)]

β exceeds unity and so ξ in (11) is limited by

$$\beta\sin\xi<1.$$

Hence there is a forbidden range of ξ, given by

$$\psi<\xi<\pi-\psi, \qquad (12)$$

in which there is no TDS. ψ lies in the first quadrant and its magnitude is arc sin $(1/\beta)$. The allowed range of ξ is

$$(\pi/2)-\theta<\xi<\psi \qquad (13)$$

for $\varepsilon=+1$, and is

$$\pi-\psi<\xi<(3\pi/2)-\theta \qquad (14)$$

for $\varepsilon=-1$. Both positive and negative roots are permissible in (11), and so there are two solutions of q for each allowed value of ξ. The edges of the 'wavelength window', as represented by (12), occur when these two solutions are identical, *i.e.* when

$$\beta\sin\xi=1 \quad \text{or} \quad \tan\xi=\varepsilon(\beta^2-1)^{-1/2}. \qquad (15)$$

The angle ξ is then equal to $\pi-\psi$ for $\varepsilon=-1$ and to ψ for $\varepsilon=+1$.

If $\beta=\sec\theta$, ψ is $(\pi/2)-\theta$ and the allowed range in (13) contracts to nothing. The allowed range in (14) becomes

$$\pi/2+\theta<\xi<3\pi/2-\theta$$

and there is now just one branch of the scattering surface with $\varepsilon=-1$ [see Fig. 8(*d*)].

We have assumed above that $\theta>\theta_B$, *i.e.* that $\Delta\theta$ is positive. If $\Delta\theta$ is negative, the signs of ε must be interchanged throughout; for example, (13) applies to $\varepsilon=-1$ and $\Delta\theta<0$.

(iii) $\beta>\sec\theta$ [*see Fig.* 8(*e*)]

As β increases beyond sec θ, there is no scattering for $\varepsilon=+1$ (with $\Delta\theta>0$). For $\varepsilon=-1$, the allowed range of ξ in (14) contracts even further:

$$\pi-\psi<\xi<\pi+\psi. \qquad (16)$$

When the neutron velocity is much less than the sound velocity, $\beta\to\infty$ and ψ [= arc sin $(1/\beta)$] $\to 0$, and so the range in (16) reduces to nothing. Thermal diffuse

scattering is then forbidden for any value of the incident wavelength.

Similarly, for $\theta < \theta_B$, the absorption process ($\varepsilon = -1$) is always forbidden, and the emission process ($\varepsilon = +1$) occurs in a smaller and smaller range of incident wavelengths as $1/\beta \to 0$.

The results given in (i) to (iii) are illustrated in Fig. 8 for the special case of $\theta = 40$ and $\Delta\theta = +6°$. The scattering surfaces have been drawn for isotropic sound velocities. Fig. 8(a), for $\beta = 0{\cdot}50$, corresponds to case (i). Any wave vector $\mathbf{k}_0$ gives rise to one-phonon scattering by both absorption and emission of phonons. Fig. 8(b), for $\beta = 1{\cdot}00$, is intermediate between (i) and (ii). There is not yet a wavelength gap, but scattering now occurs for a given k_0 either by absorption or by emission but not by both. Fig. 8(c), for $\beta = 1{\cdot}15$, represents case (ii). Here there is a wavelength window, for which TDS is forbidden, lying between the two broken lines. In Fig. 8(d), $\beta = 1{\cdot}30 = \sec\theta$; the scattering surface is a paraboloid, and the wavelength window extends indefinitely towards shorter wavelengths. Finally, Fig. 8(e) corresponds to case (iii) with $\beta = 2{\cdot}00$. One-phonon scattering occurs for a narrow band of wavelengths between the broken lines which encompass the reciprocal-lattice point, and there is no scattering outside this band.

We have shown that, provided the neutron velocity exceeds the sound velocity, there is an unbroken range of incident wavelengths which can participate in one-phonon scattering. As β increases beyond unity, the range is reduced by the appearance of forbidden regions which are associated with each reciprocal-lattice point. If β lies between unity and sec θ, there is a forbidden gap (wavelength window) near the Bragg wavelength λ_B, whereas for $\beta > \sec\theta$ there is an allowed gap near $\lambda = \lambda_B$ surrounded on either side by forbidden regions. These points are illustrated in a different way in Fig. 9 which shows the allowed ranges of the angle ξ (see Fig. 2) for the five diagrams in Fig. 8.

A wavelength window bounded by two bands of wavelengths, with one band giving thermal diffuse scattering for $\varepsilon = +1$ and the other band for $\varepsilon = -1$, occurs when the velocity ratio β lies between unity and sec θ. Thus the range of β giving a wavelength window is rather small for 2θ less than $\pi/2$, but in

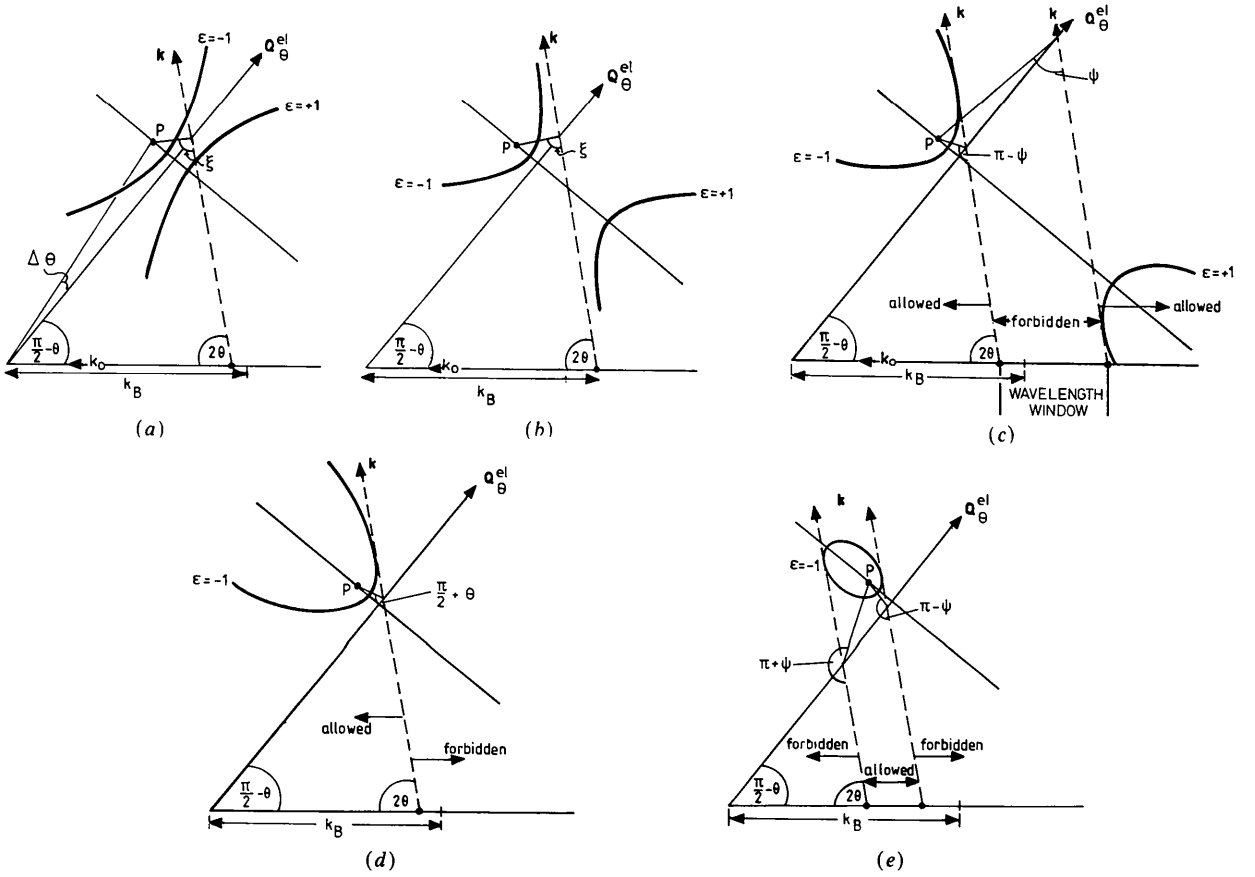

Fig. 8. Diagrams illustrating the change in the one-phonon scattering surface with increasing β, where β is the ratio of the sound velocity to the neutron velocity; (a) $\beta < 1$; (b) $\beta = 1$; (c) $1 < \beta < \sec\theta$; (d) $\beta = \sec\theta$; (e) $\beta > \sec\theta$. P is the reciprocal-lattice point and the diagrams are drawn for isotropic sound velocities and for $\theta = 40$, $\Delta\theta = +6°$. The broken lines are vectors parallel to the scattered beam; TDS takes place when these vectors intersect the scattering surfaces, indicated by heavy lines.

a back-scattering instrument the range can become very large. For example, in the time-of-flight instrument described by Steichele & Arnold (1973) θ is 88·5°, and so there is a window for all neutron velocities lying between the sound velocity c_s and one-fortieth of c_s. The HRPD instrument (Johnson & David, 1985) used in recording the diffraction patterns in Fig. 11 has detectors at even higher values of 2θ: for the highest-angle detector, sec θ is over 50.

In the rest of this paper we shall be concerned with the properties of the wavelength window in the range $1<\beta<\sec\theta$ and with the information that can be derived from it, especially as θ approaches $\pi/2$.

4. One-phonon time-of-flight cross section outside the window

Our first task is to consider the relation between the time of flight t and the wave numbers of the incident (k_0) and scattered (k) neutrons. The neutron velocity is $(\hbar/m_n)$ times the wave number, and so

$$t=(m_n/\hbar)(L_0/k_0+L/k) \tag{17}$$

where L_0 is the distance from source to sample and L the distance from sample to detector. Normally, L_0 is much larger than L: in the HRPD, $L_0/L=50$. Also, for inelastic scattering by acoustic phonons,

$$|k-k_0|\ll k_0.$$

For both these reasons (17) can be written, to a good approximation, as

$$t=\text{constant}/k_0. \tag{18}$$

Hence all elastic and inelastic events associated with the same incident wavelength $2\pi/k_0$ are integrated together into the same time channel.

The measured time-of-flight cross section is proportional to the partial differential scattering cross section

$$\left(\frac{d^2\sigma}{d\Omega\,dE}\right)^{\text{inel}}_{\text{coh}} \tag{19}$$

provided $|t-t_B|\ll t_B$, where t_B is the time for Bragg scattering. Expression (19) represents the number of neutrons coherently scattered per second in a one-phonon process into a solid angle $d\Omega$ and into an energy band $E\to E+dE$.

The cross section may be expressed as the sum of two terms, one for absorption ($\varepsilon=-1$) and the other for emission ($\varepsilon=+1$):

$$\left(\frac{d^2\sigma}{d\Omega\,dE}\right)^{\text{inel}}_{\text{coh}}=\left(\frac{d^2\sigma}{d\Omega\,dE}\right)^{\text{inel}}_{\text{coh},-1}+\left(\frac{d^2\sigma}{d\Omega\,dE}\right)^{\text{inel}}_{\text{coh},+1}.$$

The absorption term is given by equation (4.34) of Willis & Pryor (1975):

$$\left(\frac{d^2\sigma}{d\Omega dE}\right)^{\text{inel}}_{\text{coh},-1}=\frac{k}{k_0}\frac{4\pi^3}{v_0}\sum_{j\mathbf{q}}\sum_{\mathbf{B}}\left\{\frac{n_j(\mathbf{q})}{\omega_j(\mathbf{q})}\times\left|\sum_{\kappa}(b^{\text{coh}}_{\kappa}m_{\kappa}^{-1/2})\exp(-W_{\kappa})\times\exp(i\mathbf{Q}.\mathbf{r}_{\kappa})[\mathbf{Q}.\mathbf{e}(\kappa|j\mathbf{q})]\right|^2\times\delta[\omega-\omega_j(\mathbf{q})]\delta(\mathbf{Q}-\mathbf{q}-\mathbf{B})\right\}. \tag{20}$$

ω is defined by the equation

$$\hbar\omega\equiv E-E_0=(\hbar^2/2m_n)(k^2-k_0^2) \tag{21}$$

and the 'scattering vector' $\mathbf{Q}$ by

$$\mathbf{Q}=\mathbf{k}-\mathbf{k}_0.$$

Thus the first delta function in (20) represents the condition for energy conservation and the second the condition for the conservation of momentum. [The remaining symbols in (20) are defined in the glossary.]

There is a similar expression to (20) for phonon emission:

$$\left(\frac{d^2\sigma}{d\Omega dE}\right)^{\text{inel}}_{\text{coh},+1}=\frac{k}{k_0}\frac{4\pi^3}{v_0}\sum_{j\mathbf{q}}\sum_{\mathbf{B}}\left\{\frac{n_j(\mathbf{q})+1}{\omega_j(\mathbf{q})}\times\left|\sum_{\kappa}(b^{\text{coh}}_{\kappa}m_{\kappa}^{-1/2})\exp(-W_{\kappa})\times\exp(i\mathbf{Q}.\mathbf{r}_{\kappa})[\mathbf{Q}.\mathbf{e}(\kappa|j\mathbf{q})]\right|^2\times\delta[\omega+\omega_j(\mathbf{q})]\delta(\mathbf{Q}+\mathbf{q}-\mathbf{B})\right\}. \tag{22}$$

To derive the total intensity of the TDS, we must integrate the differential cross section over the phonon wave vectors $\mathbf{q}$ and over the energy E. Let us consider the absorption cross section in (20) first. The

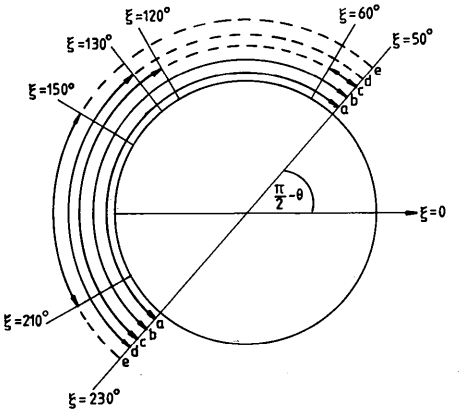

Fig. 9. Allowed ranges (full lines) and forbidden ranges (broken lines) of the angle ξ for the five values, (*a*) to (*e*), of β in Fig. 8. The entire range of ξ, $(\pi/2)-\theta<\xi<(3\pi/2)-\theta$, is allowed in *a* and *b*, but the allowed range is successively reduced as β is increased beyond unity from *c* to *d* to *e*.

integration over $\mathbf{q}$ is performed by multiplying by the density of $\mathbf{q}$ vectors in reciprocal space, which is $Nv_0/8\pi^3$ where N is the number of unit cells in the crystal. Thus

$$\left(\frac{d^2\sigma}{d\Omega\, dE}\right)^{\text{inel}}_{\text{coh},-1} = \frac{k}{k_0}\frac{N}{2}\sum_j \left\{\delta[\omega-\omega_j(\mathbf{q})]\frac{n_j(\mathbf{q})}{\omega_j(\mathbf{q})} \times|(b_\kappa^{\text{coh}} m_\kappa^{-1/2})\exp(-W_\kappa) \times\exp(i\mathbf{Q}.\mathbf{r}_\kappa)[\mathbf{Q}.\mathbf{e}(\kappa|j\mathbf{q})]|^2\right\}. \tag{23}$$

In this equation it is understood that, for each branch j, $\mathbf{q}$ and $\mathbf{B}$ are related by

$$\mathbf{Q}=\mathbf{B}+\mathbf{q}.$$

The integration over the energy E in (23) is more difficult, because the phonon energy $\hbar\omega_j(\mathbf{q})$ in the argument of the delta function is itself a function of ω. If $\text{grad}_\mathbf{q}$ is the gradient with respect to the direction of $\mathbf{q}$, we have from (21) that

$$\frac{\partial}{\partial E}[\omega-\omega_j(\mathbf{q})] = -\frac{1}{\hbar}+\frac{1}{2E}\mathbf{k}.\text{grad}_\mathbf{q}[\omega_j(\mathbf{q})].$$

[$|\text{grad}_\mathbf{q}\omega_j(\mathbf{q})|$ is the group velocity of the acoustic waves or the velocity of energy transmission.] With

$$|J_{-1}| = 1-(\hbar/2E)\mathbf{k}.\text{grad}_\mathbf{q}[\omega_j(\mathbf{q})] \tag{24}$$

and

$$G_j(\mathbf{Q}) = \sum_\kappa \frac{b_\kappa^{\text{coh}}}{m_\kappa^{1/2}}\exp(-W_\kappa)\exp(i\mathbf{Q}.\mathbf{r}_\kappa)[\mathbf{Q}.\mathbf{e}(\kappa|j\mathbf{q})] \tag{25}$$

inserted into (23) integration over E gives the differential cross section:

$$\left(\frac{d\sigma}{d\Omega}\right)^{\text{inel}}_{\text{coh},-1} = \frac{k}{k_0}\frac{N}{2}\sum_j \frac{n_j(\mathbf{q})}{\omega_j(\mathbf{q})}|G_j(\mathbf{Q})|^2|J_{-1}|^{-1}. \tag{26}$$

Expression (25) for $G_j(\mathbf{Q})$, the 'structure factor for one-phonon scattering', can be simplified by recalling that we are concerned only with low-frequency acoustic modes for which the polarization vector $\mathbf{e}(\kappa|j\mathbf{q})$ is the same for all atoms κ in the unit cell. Thus

$$|G_j(\mathbf{Q})|^2 = |\mathbf{Q}.\mathbf{e}(j\mathbf{q})|^2|F(\mathbf{Q})|^2 \tag{27}$$

where the eigenvector $\mathbf{e}(j\mathbf{q})$ has been mass adjusted to include $m_\kappa^{-1/2}$ in (25) and $F(\mathbf{Q})$ is the structure factor for Bragg scattering:

$$F(\mathbf{Q}) = \sum_\kappa b_\kappa^{\text{coh}}\exp(-W_\kappa)\exp(i\mathbf{Q}.\mathbf{r}_\kappa).$$

The quantum number of the mode is

$$n_j(q) = \{\exp[\hbar\omega_j(\mathbf{q})/k'_BT]-1\}^{-1}$$

where k'_B is Boltzmann's constant and T the absolute temperature. In the classical regime, $k'_BT \gg \hbar\omega(\mathbf{q})$ and so

$$n_j(\mathbf{q}) = k'_BT/\hbar\omega_j(q). \tag{28}$$

Substitution of (27) and (28) into (26) gives the final result:

$$\left(\frac{d\sigma}{d\Omega}\right)^{\text{inel}}_{\text{coh},-1} = \frac{k}{k_0}\frac{N}{2}\frac{k'_BT}{\hbar} \times\sum_j[\omega_j(\mathbf{q})]^{-2}|\mathbf{Q}.\mathbf{e}(j\mathbf{q})|^2|F(\mathbf{Q})|^2|J_{-1}|^{-1}. \tag{29}$$

There is a similar equation for the emission cross section:

$$\left(\frac{d\sigma}{d\Omega}\right)^{\text{inel}}_{\text{coh},+1} = \frac{k}{k_0}\frac{N}{2}\frac{k'_BT}{\hbar} \times\sum_j[\omega_j(\mathbf{q})]^{-2}|\mathbf{Q}.\mathbf{e}(j\mathbf{q})|^2|F(\mathbf{Q})|^2|J_{+1}|^{-1} \tag{30}$$

where

$$|J_{+1}| = 1+(\hbar/2E)\mathbf{k}.\text{grad}_\mathbf{q}[\omega_j(\mathbf{q})]. \tag{31}$$

Equations (29) and (30) give the one-phonon scattering cross sections which are measured in a time-of-flight diffraction experiment. The principal components of these expressions are the frequency, polarization and Jacobian terms.

(i) *The frequency term*, $[\omega_j(\mathbf{q})]^{-2}$

For acoustic modes propagating without dispersion, the frequency $\omega_j(\mathbf{q})$ is proportional to q. Hence the frequency term gives an intensity which varies as $1/q^2$: near the centre of the Brillouin zone, $q\to 0$ and the intensity $\to\infty$. This is the origin of the well known TDS error in the measurement of Bragg intensities.

(ii) *The polarization term*, $|\mathbf{Q}.\mathbf{e}(j\mathbf{q})|^2$

If the elastic wave is polarized at right angles to the direction of the scattering vector $\mathbf{Q}$, the polarization term is zero and the wave contributes nothing to the TDS. This term is useful, therefore, in identifying the type of acoustic branch ($j=1, 2, 3$) contributing to the scattering.

(iii) *The Jacobian term*, $|J|^{-1}$

The Jacobian J is given by

$$J = 1+(\varepsilon\hbar/2E)\mathbf{k}.\text{grad}_\mathbf{q}[\omega_j(\mathbf{q})]. \tag{32}$$

If χ is the angle between the gradient of $\omega_j(\mathbf{q})$ and the scattered neutron, then

$$\mathbf{k}.\text{grad}_\mathbf{q}[\omega_j(\mathbf{q})] = kc_g\cos\chi$$

where c_g is the group velocity. If we write

$$\beta_g = c_g/v_n,$$

(32) becomes

$$J = 1 + \varepsilon\beta_g \cos\chi$$

so that J is zero when

$$\beta_g \cos\chi = -\varepsilon. \tag{33}$$

Thus the absorption cross section, (29), rises to a peak when $\beta_g \cos\chi = +1$, and the emission cross section, (30), to a peak when $\beta \cos\chi = -1$.

The frequency term (i) also leads to a maximum in the TDS intensity, but this is obscured by the Bragg peak. The Jacobian term gives peaks for $\varepsilon = \pm 1$, which are displaced from the Bragg position and are readily observed with neutrons [see Fig. 11(b)]. They cannot be observed with X-rays as $1/J$ is close to unity.

To examine the relationship between the position of the TDS peak and the wavelength at the edge of the window, it is convenient to describe the phonon wave vector $\mathbf{q}$ in polar coordinates (q, ζ). The group velocity c_g is

$$\text{grad}\,\omega(q,\zeta) = \mathbf{e}_q \partial\omega/\partial q + \mathbf{e}_\zeta (1/q)(\partial\omega/\partial\zeta)$$

with $\mathbf{e}_q$ and $\mathbf{e}_\zeta$ representing unit vectors along and perpendicular to $\mathbf{q}$. The phase velocity, in the absence of dispersion, is

$$c_s = \partial\omega/\partial q.$$

Thus

$$\beta_g^2 = \beta^2 + \beta'^2$$

where β' is $\mathrm{d}\beta/d\zeta$.

After some algebra and with the aid of the expression above, we find that (33) is equivalent to

$$\tan\xi = \varepsilon(\beta^2 + \beta'^2 - 1)^{-1/2}.$$

If $\beta' = 0$, *i.e.* if the crystal is elastically isotropic, this expression reduces to (15), which defines the edges of the wavelength window. For the isotropic case, the intensity at the edges rises abruptly from nothing to a large value for an infinitesimal change in the incident wavelength. This is illustrated schematically in Fig. 10(b). Note that the group velocity is the same as the phase velocity provided *both* dispersion and anisotropy are zero.

The singularities in the TDS cross section are analogous to those giving critical points in the spectrum of vibrational frequencies (Van Hove, 1953). Van Hove singularities occur at those frequencies for which the group velocity, $\text{grad}_\mathbf{q}[\omega(\mathbf{q})]$, vanishes in some direction. In our case the singularities appear when the group velocity is equal to $v_n \sec\chi$.

5. Width of the window

From the results in § 3 we can calculate the width of the wavelength window as a function of the offset angle $\Delta\theta$.

Turning to Fig. 2, where $OP = 2k_B \sin\theta_B$ and $OS = 2k_0 \sin\theta$, we get

$$(k_0 \sin\theta)/(k_B \sin\theta_B) = \sin(\alpha + \theta - \theta_B)/\sin\alpha \tag{34}$$

where $\alpha = \xi - (\pi/2) + \theta$. If we put $\Delta k_0 = k_0 - k_B$ and $\Delta\theta = \theta - \theta_B$, where $\Delta k_0 \ll k_B$ and $\Delta\theta \ll \theta_B$, (34) becomes

$$\Delta k_0/k_B = (\cot\alpha - \cot\theta_B)\,\Delta\theta. \tag{35}$$

At the edge of the window [see (15)]

$$\tan\xi = \varepsilon(\beta^2 - 1)^{-1/2}$$

and so

$$\frac{\Delta k_0}{k_B} = \frac{\Delta\theta\,\text{cosec}^2\,\theta}{\varepsilon'(\beta^2-1)^{-1/2} - \cot\theta} \tag{36}$$

where the expression has been generalized to cover all combinations of ε and $\Delta\theta/|\Delta\theta|$. Equation (36) gives the wave number of the incident radiation at the two edges of the window. For positive $\Delta\theta$, Δk_0 is positive for phonon emission and negative for absorption; for negative $\Delta\theta$, the signs of Δk_0 are reversed. If β^2 in (36) is replaced by $\beta^2 + \beta'^2$, the resultant Δk_0 corresponds to the position of the TDS peak: see § 4.

Equation (36) has been used to calculate $\Delta t/t_B$ $(= -\Delta k_0/k_B)$ for the three cases illustrated in Figs. 8(b), (c) and (d): these calculated times are indicated by vertical arrows in Fig. 10. Figs. 10(a) and (c) represent the minimum and maximum values of β for the range $1 < \beta < \sec\theta$; (b) is in the middle of the range and shows that, for $2\theta = 80°$, the wavelength window is asymmetric with respect to t_B. Note that

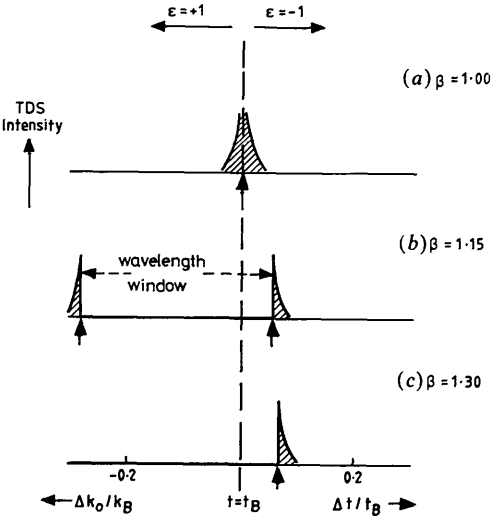

Fig. 10. Variation of TDS intensity with time of flight (schematic). The three cases have been drawn for $\theta = 40$ and $\theta_B = 34°$. (a) and (c) correspond to the two extremes and (b) to the centre of the range $1 < \beta < \sec\theta$. Note that the wavelength window in (b) is asymmetric with respect to the Bragg position at $t = t_B$.

energy gain occurs for the slower neutrons and energy loss for the faster neutrons.

To define the phonon at the edge of the window, expressions are required for both the magnitude and the direction of **q**. Putting $\beta \sin \xi = 1$ and $\beta \cos \xi = \varepsilon(\beta^2-1)^{1/2}$ into (11), the magnitude of **q** is

$$q = \eta(\beta^2-1)^{-1/2} \tag{37}$$

where η is the length of the vector $\overline{PS}$ in Fig. 2. But

$$(\eta/2)^2 = \Delta\theta^2 k_B^2 + \Delta k_0^2 \sin^2\theta_B + \Delta\theta\,\Delta k_0\, k_B \sin(2\theta_B)$$

and combination of this with (36) and (37) gives the general expression for q:

$$q = \frac{\beta}{(\beta^2-1)} \frac{2k_B|\Delta\theta|}{(\beta^2-1)^{-1/2} - \varepsilon' \cot\theta}. \tag{38}$$

The direction of **q** is determined by the angle ζ between **q** and the fixed vector **B**. From (15) and Fig. 2(*b*)

$$\zeta = \theta + \varepsilon' \arcsin(1/\beta) \tag{39}$$

where arc sin $(1/\beta)$ lies in the first quadrant and it is assumed that $\Delta\theta \ll \theta_B$.

Equations (38) and (39) show that the two sides of the wavelength window, with $\varepsilon = -1$ and $\varepsilon = +1$, correspond to phonons which differ in both magnitude and direction. However, the *same phonon* is observed at the absorption (emission) edge for $\Delta\theta > 0$ as is observed at the emission (absorption) edge for a negative offset angle of the same magnitude.

The asymmetry between the two edges of the window decreases with increasing θ and disappears at $\theta = \pi/2$. Equation (36) then reduces to

$$\Delta k_0/k_B = -\Delta t/t_B = \varepsilon'(\beta^2-1)^{1/2}|\Delta\theta|$$

and the absorption and emission edges are symmetrically displaced in time on either side of $t = t_B$. The total width of the window for $\theta = \pi/2$ is

$$\Delta t_{\text{tot}} = 2t_B(\beta^2-1)^{1/2}\Delta\theta \tag{40}$$

and the wave numbers of the phonons at the cut-off wavelengths are

$$q(\zeta) = \beta(\beta^2-1)^{-1/2} 2k_B|\Delta\theta|$$

where the propagation direction is given by

$$\zeta = (\pi/2) + \varepsilon' \arcsin(1/\beta). \tag{41}$$

The range of β is $1 < \beta < \sec\theta$. At the extreme ends of this range, (41) gives $\zeta = 0$ and π for $\beta = 1$, and $\zeta = \pi/2$ for $\beta \gg 1$. Hence, on account of the polarization term $|\mathbf{Q}.\mathbf{e}(j\mathbf{q})|^2$ in the cross sections in (29) and (30), TDS peaks arising from transverse modes of vibration will not be seen in back scattering when β is close to unity and peaks from longitudinal modes will not be seen when β is very large and close to sec θ.

6. Measurement of sound velocities in pyrolytic graphite

To illustrate the concepts given above, we shall describe the interpretation of experimental data on pyrolytic graphite, which were obtained using the high-resolution powder diffractometer (HRPD) at the spallation neutron source ISIS. Fig. 11(*a*) shows the 00*l* Bragg peaks, recorded at a scattering angle 2θ of 174·6°; in Fig. 11(*b*) 2θ has been increased to 177·8° and each Bragg peak is now replaced by a pair of one-phonon peaks, one due to absorption and the other to emission.

θ is nearly 90°, and so the window is symmetrical about $t = t_B$ and (40) can be used to evaluate $\beta(\zeta)$ and $c_s(\zeta)$ as a function of the direction of propagation. The steps in the calculation are given in Table 1. The last two columns show that the phase velocity rises steeply as the direction approaches the normal to the close-packed layers.

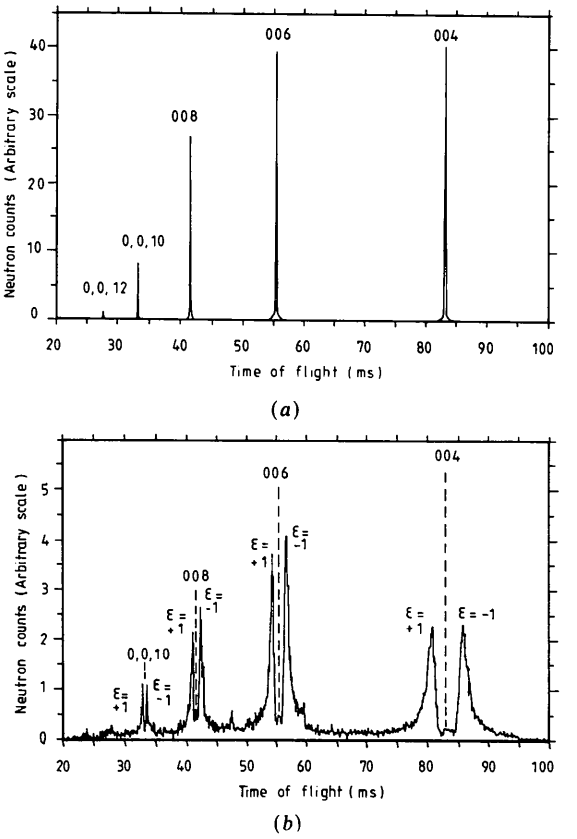

Fig. 11. (*a*) Time-of-flight neutron diffraction pattern of pyrolytic graphite, taken with the high-resolution powder diffractometer, HRPD. The scattering angle was $2\theta = 2\theta_B$ where $\theta_B = 87{\cdot}3°$. The 00*l* Bragg peaks are labelled 004 to 0,0,12. (002 is excluded because of frame overlap.) (*b*) Time-of-flight pattern taken under the same conditions as (*a*) apart from 2θ being increased by $2\Delta\theta$ where $\Delta\theta = 1{\cdot}6°$. The 00*l* Bragg positions, as derived from (*a*), are indicated by broken lines. Each position is flanked symmetrically by lines for phonon absorption ($\varepsilon = -1$) and phonon emission ($\varepsilon = +1$). (After Willis *et al.*, 1986.)

Table 1. *Sound velocities in graphite*

See Fig. 11(*b*): $\theta = 88{\cdot}93$ and $\Delta\theta = +1{\cdot}63°$.

00*l*	Δt_{tot} (ms)	t_B (ms)	$\beta(\zeta)$	v_n (km s^{-1})	$c_s(\zeta)$ (km s^{-1})	ζ (°)
004	6·46	83·05	1·693	1·17	1·98	53·7
006	2·78	55·33	1·334	1·75	2·33	41·4
008	1·54	41·50	1·193	2·34	2·79	33·1
0,0,10	0·85	33·19	1·096	2·92	3·20	24·2

Table 2. *Magnitudes of wave vectors, expressed as a fraction of the wave vector for Bragg scattering*

00*l*	q/k_B	$\Delta k_0/k_B$	$\Delta k/k_B$
004	0·070	−0·038	0·080
006	0·085	−0·025	0·088
008	0·104	−0·018	0·106
0,0,10	0·139	−0·012	0·140

In graphite (Bowman & Krumhansl, 1958) the acoustic modes have polarization vectors which are either within the layers ('in-plane modes') or normal to the layers ('out-of-plane modes'). In the present experiment, scattering from the in-plane modes was suppressed by the polarization factor $|\mathbf{Q}.\mathbf{e}(j\mathbf{q})|^2$, and only the out-of-plane modes were observed.

Table 2 gives the magnitudes of q, Δk_0 and Δk at the absorption edge ($\varepsilon = -1$) of the wavelength window, as calculated from the expressions in § 5.

The quantity

$$(\Delta k + \Delta k_0)/2k_B$$

lies between 0·02 and 0·065, so that there is an error of about 4% in the sound velocities quoted in Table 1, which arises from neglecting $(\Delta k + \Delta k_0)$ in (4). In the analysis of the same data by Willis, Carlile, Ward, David & Johnson (1986) this error was eliminated by extrapolating the results to $\Delta\theta = 0$.

Many of the ideas developed in this paper were discussed initially with Dr C. J. Carlile of the Rutherford Appleton Laboratory and with Dr P. Schofield of AERE, Harwell. The experimental measurements were carried out on the pulsed neutron source ISIS of the Rutherford Appleton Laboratory. The author is grateful for the hospitality of Dr C. K. Prout, Head of the Chemical Crystallography Laboratory, Oxford.

References

BOWMAN, J. C. & KRUMHANSL, J. A. (1958). *J. Phys. Chem. Solids*, **6**, 367-379.
ELLIOTT, R. J. & LOWDE, R. D. (1955). *Proc. R. Soc. London. Ser. A*, **230**, 46-73.
JOHNSON, M. W. & DAVID, W. I. F. (1985). Rutherford Appleton Lab. Rep. RAL-85-112.
SEEGER, R. J. & TELLER, E. (1942). *Phys. Rev.* **62**, 37-40.
STEICHELE, E. & ARNOLD, P. (1973). *Phys. Lett. A*, **44**, 165-166.
VAN HOVE, L. (1953). *Phys. Rev.* **89**, 1189-1193.
WILLIS, B. T. M., CARLILE, C. J., WARD, R. C., DAVID, W. I. F. & JOHNSON, M. W. (1986). *Europhys. Lett.* In the press.
WILLIS, B. T. M. & PRYOR, A. W. (1975). *Thermal Vibrations in Crystallography*. Cambridge Univ. Press.

Acta Cryst. (1986). A**42**, 525-533

A New Approach to Multibeam X-ray Diffraction Using Perturbation Theory of Scattering

BY QUN SHEN

Department of Physics, Purdue University, West Lafayette, Indiana 47907, *USA*

(*Received* 8 *March* 1986; *accepted* 23 *May* 1986)

Abstract

Perturbations to conventional two beam X-ray diffraction arising from multibeam scattering effects have been studied theoretically. A simple analytical expression for the diffracted wave field and intensity near a multiple excitation is derived by using the perturbation theory of scattering of electromagnetic waves. Although it cannot be applied to the center of a multibeam diffraction peak, it does show explicitly the asymmetry effect observed in experiments and its phase dependence in the neighborhood of the multibeam point. A numerical calculation for the $\bar{1}1\bar{1}$ *Umweganregung* peak on the almost-forbidden 442 reflection of silicon gives excellent agreement with experimental data and exact n-beam computer calculations based on conventional dynamical theory. From the analytical expression, a simple rule is derived for phase determination in centrosymmetric crystals. A general 'pseudo-four-beam' case where no asymmetry effect exists is also discussed as another example of the applications.

0108-7673/86/060525-09$01.50